

Energy-efficient field-free unconventional spin-orbit torque magnetization switching dynamics in van der Waals heterostructures

Lalit Pandey^{1,2}, Bing Zhao¹, Roselle Ngaloy¹, Himanshu Bangar¹, Aya Ali³, Mahmoud Abdel-Hafiez^{3,4}, Gaojie Zhang⁵, Hao Wu⁵, Haixin Chang⁵, Lars Sjöström¹, Prasanna Rout¹, Saroj P. Dash^{1,2,6*}

¹Department of Microtechnology and Nanoscience, Chalmers University of Technology, SE-41296, Göteborg, Sweden.

²Wallenberg Initiative Materials Science for Sustainability, Department of Microtechnology and Nanoscience, Chalmers University of Technology, SE-41296, Göteborg, Sweden.

³Department of Applied Physics and Astronomy, University of Sharjah, Sharjah, United Arab Emirates.

⁴Department of Physics and Astronomy, Uppsala University, Box 516, SE-751 20 Uppsala, Sweden.

⁵School of Materials Science and Engineering, Huazhong University of Science and Technology, 430074, Hubei, China,

⁶Graphene Center, Chalmers University of Technology, SE-41296, Göteborg, Sweden.

Abstract

The van der Waals (vdW) heterostructure of emerging two-dimensional (2D) quantum materials, with control over their quantum geometries, crystal symmetries, spin-orbit coupling, and magnetic anisotropies, provides a new platform for generating unconventional nonlinear Hall effects, spin polarization and efficiently controlling the magnetization dynamics for non-volatile spin-based computing. However, so far, the generation of a large out-of-plane spin polarization is limited to achieve energy-efficient field-free magnetization switching and spin dynamics measurements in all-2D vdW heterostructure are so far missing, where the interplay between spins and magnetization dynamics should enable the design of ultrafast spintronic devices. Here, we demonstrate magnetization dynamics and energy-efficient field-free spin-orbit torque (SOT) switching of out-of-plane magnet Fe_3GaTe_2 due to unconventional Berry curvature-induced out-of-plane spin polarization from a topological Weyl semimetal TaIrTe_4 in a vdW heterostructure at room temperature. We observed a large non-linear 2nd harmonic Hall signal at room temperature and evaluated the SOT-induced magnetization dynamics with a large damping-like torque of 4.83 ± 0.59 mT per MAcm^{-2} . Deterministic field-free SOT magnetization switching in vdW heterostructure of $\text{TaIrTe}_4/\text{Fe}_3\text{GaTe}_2$ is observed at room temperature with a low current and power density of 1.81×10^{10} A/m² and 0.175×10^{15} $\frac{\text{W}}{\text{m}^3}$, respectively, which is an order of magnitude better than that of conventional systems. From the magnetization switching experiments, the SOT efficiency is found to be 3.95 with a very large spin Hall conductivity of $7.39 \times 10^6 \hbar/2e$ (Ωm)⁻¹. These findings on all-vdW heterostructures offer a promising route to energy-efficient and external field-free ultrafast spintronic technologies.

Keywords: Quantum materials, Berry curvature, Broken symmetries, Spin-orbit torque (SOT), magnetization dynamics, van der Waals materials, Weyl semimetals, 2D ferromagnets, Unconventional SOT, 2D materials, Room temperature, 2nd Harmonics, TaIrTe_4 , Fe_3GaTe_2

Corresponding author: Saroj P. Dash, Email: saroj.dash@chalmers.se

Introduction

The interplay of spin-orbit coupling and magnetism with control over the band topology, quantum geometries and crystal symmetries provides emerging properties of quantum materials and holds promise for next-generation universal memory and computing technologies^{1,2}. Specifically, spin-orbit torque (SOT) phenomena leverage charge-spin conversion (CSC) in such quantum materials with large spin-orbit coupling (SOC), Berry curvature and topological spin textures to induce a magnetization switching of an adjacent ferromagnet (FM)³. In conventional SOT devices, the commonly used spin-orbit materials (SOM) exhibit moderate CSC efficiency and provide an in-plane SOT torque component, limiting their application in switching a magnet with perpendicular magnetic anisotropy (PMA)⁴.

van der Waals (vdW) heterostructures composed of two-dimensional (2D) materials offer a new framework to address the aforementioned fundamental challenges in SOT technologies⁵. vdW SOMs^{6,7}, with lower crystal symmetries provide the generation of an out-of-plane SOT, which is suitable for field-free switching of a magnet with PMA. On the other hand, vdW magnets with a strong PMA above room temperature for reliable SOT device operations^{8,9}. Taking advantage of such materials, all-2D vdW heterostructures have been reported for field-free SOT switching¹⁰⁻¹⁴. However, the SOT switching efficiency is two to three orders of magnitude lower than required for energy-efficient switching. To circumvent these issues, recently, a Weyl semimetal TaIrTe₄ with lower crystal symmetry, canted topological spin textures and large Berry curvature dipole at room temperature was explored for higher energy efficiency and field-free SOT switching of a conventional magnets^{6,15-19}. Therefore, an all-2D vdW heterostructure designed using the combination of the best vdW quantum materials with a large current-induced out-of-plane spin polarization and above room temperature vdW ferromagnet with an out-of-plane magnetization is a promising candidates for tunable, compact and energy-efficient non-volatile spintronic technologies^{1,6,12,15-18,20-24}. Furthermore, the investigation of non-linear Hall effects and spin dynamics in all-2D vdW heterostructure to understand the interplay between broken interfacial symmetries, spins and magnetization dynamics, enabling the design of more efficient and ultrafast spintronic devices is so far missing.

Here, we demonstrate energy-efficient field-free deterministic SOT magnetization switching at room temperature using the all-vdW heterostructure of TaIrTe₄/Fe₃GaTe₂. We utilized Weyl semimetal candidate TaIrTe₄ showing a large nonlinear Hall effect with a canted spin polarization of $-(27 \pm 0.76)^\circ$ at room temperature together with a vdW ferromagnet Fe₃GaTe₂ with strong PMA and T_C significantly above room temperature. The interaction between the current-induced spin polarization in TaIrTe₄ and the magnetization of the vdW magnet Fe₃GaTe₂ provides information about magnetization dynamics and SOT efficiency. Evaluation of magnetization dynamics using a detailed magnetic field and angle-dependent 2nd harmonics measurements in TaIrTe₄/Fe₃GaTe₂ all-vdW heterostructure shows a large SOT efficiency of 3.95 and a large spin Hall conductivity of $7.39 \times 10^6 \hbar/2e (\Omega\text{m})^{-1}$ at room

temperature which is much better than previous reports. Ultimately, we observed a field-free deterministic SOT magnetization switching with a very low critical switching current density of $1.81 \times 10^{10} \text{A/m}^2$, demonstrating energy-efficient non-volatile spintronic memory devices.

Results and discussion

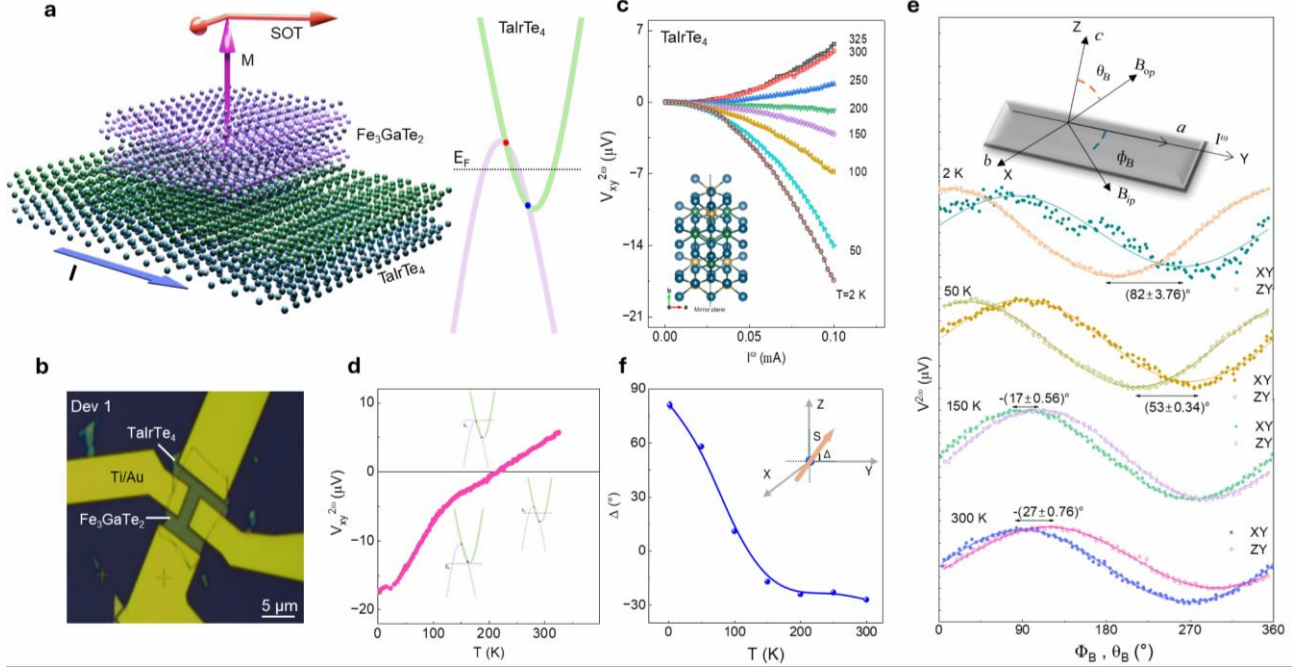


Figure 1. Van der Waals heterostructure of TaIrTe₄/Fe₃GaTe₂ and harmonic measurements on TaIrTe₄. **a.** Schematic diagram of a van der Waals heterostructure of Weyl semimetal TaIrTe₄ and out-of-plane ferromagnet Fe₃GaTe₂. Band structure of typical type-II Weyl semimetal with two Weyl fermionic nodes. **b.** Optical image of TaIrTe₄/Fe₃GaTe₂ vdW heterostructure Hall bar device with a scale bar of 5 μm. **c.** 2nd harmonic transverse Hall voltage $V_{xy}^{2\omega}$ in response to an applied alternating current I^ω along a-axis at different temperatures for a device with 20 nm TaIrTe₄. The inset illustrate the crystal structure of T_d-TaIrTe₄, characterized by reduced crystal symmetry and a mirror plane along the crystallographic a-axis. **d.** 2nd harmonic transverse Hall voltage $V_{xy}^{2\omega}$ with temperature at an I^ω of 0.1 mA of TaIrTe₄. Insets show the energy dispersion curve of type-II Weyl semimetal and tuning of Fermi level energy (E_F) with temperature. **e.** 2nd harmonic longitudinal voltage $V^{2\omega}$ response measured in TaIrTe₄ device as a function of angle between current applied along a-axis of TaIrTe₄ ($|I^\omega| = 0.1 \text{ mA}$) and external magnetic field (13 T). The device is rotated in XY and ZY planes, as depicted in schematics. In the XY rotation, the device rotates such that the magnetic field align parallel to the sample surface and making Φ_B angle with a-axis of TaIrTe₄, whereas in ZY rotation, the device rotation changes magnetic field direction from a-axis of TaIrTe₄ to c axis and making θ_B angle with c-axis with TaIrTe₄. The solid lines are the fits. **f.** Temperature dependence of shift (Δ) in the maxima or minima of $V^{2\omega}$ vs Φ_B and θ_B curves. This shift is denoted as out-of-plane spin-polarized canting angles as illustrated in schematics. Such shift is directly correlated to the out-of-plane spin canting angle which is estimated to be $-(27 \pm 0.76)^\circ$ at room temperature.

We investigated TaIrTe₄/Fe₃GaTe₂ vdW heterostructures (Fig. 1a) based on their promising properties, with the expectation that their combination could give rise to new phenomena, including large non-linear Hall effects and spin-orbit torque (SOT) magnetization dynamics. TaIrTe₄ represents a promising vdW topological Weyl semimetal (WSM) candidate, with a significant Berry curvature dipole and distinct chiral spin textures in its electronic bands, associated with both bulk Weyl nodes and Fermi-arc surface states²⁵. Such unique properties provide unconventional charge-spin conversion with an out-of-plane spin polarization component that can induce an out-of-plane SOT on the adjacent PMA ferromagnet to

induce a magnetic field-free switching. On the other hand, Fe_3GaTe_2 is a unique vdW topological nodal line metallic ferromagnet with strong PMA above room temperature with Curie temperature (T_c) around 370 K⁸.

We fabricated $\text{TaIrTe}_4/\text{Fe}_3\text{GaTe}_2$ vdW heterostructures based Hall-bar devices and the individual Hall bars on TaIrTe_4 and Fe_3GaTe_2 crystals to characterize their properties such as anomalous Hall effect (AHE), 2nd Harmonics measurements and SOT switching experiments (see detailed in the Methods section and supplementary Fig. S1). Figure 1b shows an typical optical microscope image of a representative $\text{TaIrTe}_4/\text{Fe}_3\text{GaTe}_2$ vdW heterostructure Hall-bar device. TaIrTe_4 is expected to show a large non-linear Hall effect because of the large Berry curvature dipole with strong spin-orbit coupling and inversion-symmetry breaking. We measured a strong nonlinear Hall effect in TaIrTe_4 (Fig. 1c), characterized by a 2nd harmonic Hall voltage nonlinearly dependent on driving currents sourced along the a-axis of the crystal mirror plane at room temperature. In contrast to linear Hall effects in systems with broken time-reversal symmetry, the nonlinear Hall effect in TaIrTe_4 relies on large Berry curvature, topological spin textures and broken inversion symmetry. The sign of the nonlinear Hall voltage is observed to change at ~ 150 K (Fig. 1c and 1d), which is related to the change in the Fermi energy and Fermi surface with temperature that indicates the Weyl semi-metallic properties of TaIrTe_4 ²⁶. The information about the spin texture present in TaIrTe_4 can be probed using the bilinear magnetoelectric resistance technique (BMR)²⁷, where the 2nd harmonic voltage is measured while rotating the samples in two planes (XY and ZY) as shown in Fig. 1e. In XY rotation, the magnetic field vector remains in the ab crystallographic plane sweeping azimuthal angle (Φ_B) with respect to the a-axis of TaIrTe_4 , whereas in ZY rotation, the field vector sweeps polar angle (θ_B) with respect to the c-axis of TaIrTe_4 in the ac plane. Figure 1e depicts the temperature dependence of 2nd harmonic voltage with Φ_B and θ_B . The direction of resultant spin angular momentum arises (σ) due to charge-spin conversion effects in TaIrTe_4 being equivalent to angular shift (Δ) of BMR curves measured along XY and ZY geometries. The Δ is found to be $-(27 \pm 0.76)^\circ$ at room temperature, indicating the presence of an out-of-plane spin polarization component in TaIrTe_4 . Such spin-polarization can help in generating unconventional out-of-plane SOT in adjacent ferromagnetic layer Fe_3GaTe_2 with PMA resulting in field-free deterministic switching. The temperature dependence of Δ , shown in Fig. 1f, suggests that the polarity and magnitude of the spin texture in TaIrTe_4 are highly influenced by the position of chemical potential/Fermi level²⁸.

To verify the magnetic property and anisotropy of Fe_3GaTe_2 , the anomalous Hall resistance R_{xy} is measured at different temperatures ranging from 2 to 300 K (Fig. 2a, b). A square-shaped magnetic hysteresis loop is observed with coercivity around 100 mT and anomalous Hall resistance (R_{AHE}) of around 1.5 Ω at room temperature, where the latter is directly proportional to saturation magnetization

(M_s) of Fe_3GaTe_2 . The R_{AHE} vs T curve, shown in Fig. 2c, is fitted with $M_s(T) = M_s(0) \left(1 - \left(\frac{T}{T_c}\right)^2\right)^\beta$ to estimate Curie temperature ($T_c = 369.14 \pm 7.73$ K) and critical magnetization exponent $\beta = 0.35$ ^{8,29}.

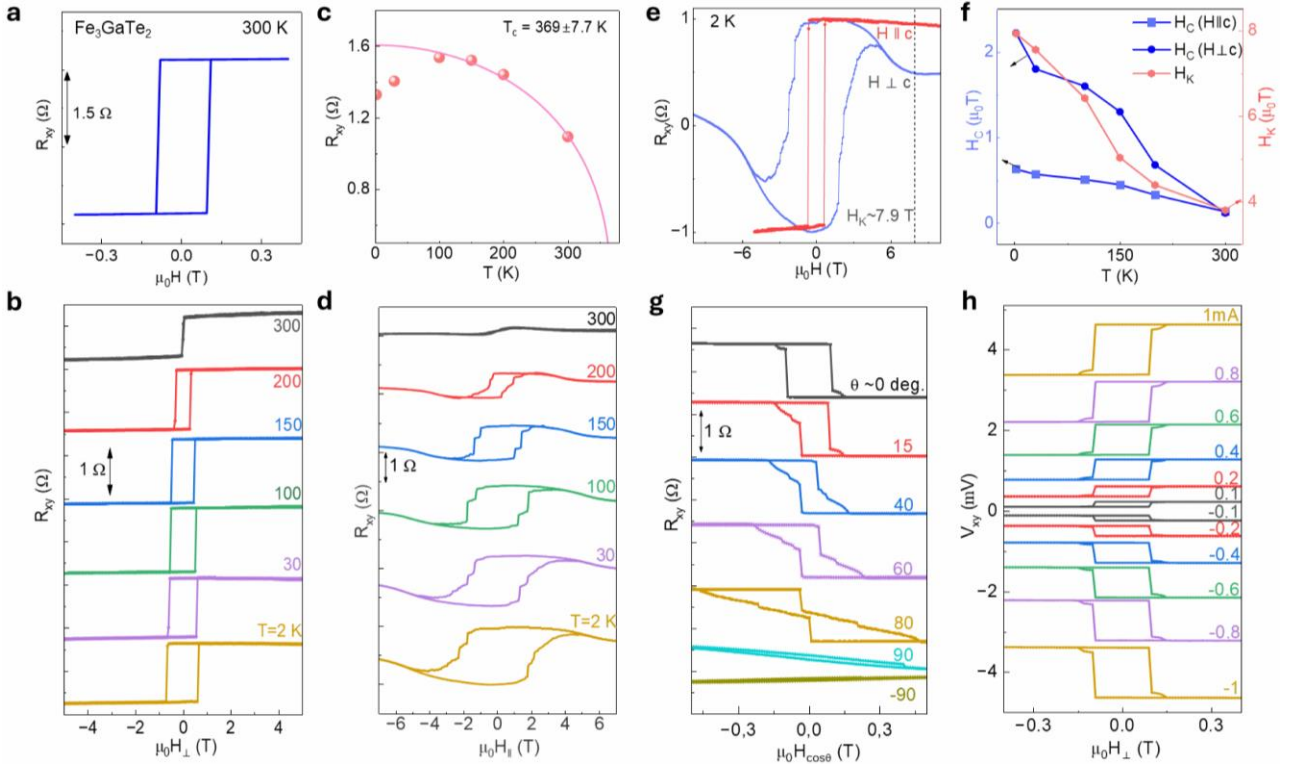


Figure 2. Magneto-transport characterization of Fe_3GaTe_2 . **a,b**, Anomalous Hall resistance of Fe_3GaTe_2 as a function of out-of-plane magnetic fields at 300 K and temperature dependence ranging from 2 to 300 K. **c**. Anomalous Hall amplitude at the saturated field as a function temperature, fitted with $M_s(T) = M_s(0) \left(1 - \left(\frac{T}{T_c}\right)^2\right)^\beta$ to extract the Curie temperature ($T_c = 369.14 \pm 7.73$ K) and critical magnetization exponent $\beta = 0.35$ ^{8,29}. **d**. Anomalous Hall resistance of Fe_3GaTe_2 as a function of in-plane magnetic fields at different temperatures ranging from 2 to 300 K. **e**. Comparison of Anomalous Hall effect measurement for field swept parallel to sample plane (i.e., $H \perp c$) vs perpendicular (i.e., $H \parallel c$) to sample plane at 2 K temperature. The anisotropic field (H_k) is ~ 7.9 T, indicating strong perpendicular magnetic anisotropy present in Fe_3GaTe_2 . **f**. Variation of coercive fields and anisotropic fields with temperature extracted from (R_{xy} vs $\mu_0 H_{\perp}$) and (R_{xy} vs $\mu_0 H_{\parallel}$) measurements. **g**. AHE signals R_{xy} with different out-of-plane angles (θ) between the magnetic field and the c -axis of the sample plane at 300 K. **h**. Variation of AHE signals R_{xy} with positive and negative DC bias currents.

Figure 2d shows the anomalous Hall resistance of Fe_3GaTe_2 as a function of in-plane magnetic fields at different temperatures from 2 to 300 K. A magnetic hysteresis loop is observed at all temperatures, with finite remanence and coercivity, consistent with the typical behavior of PMA magnets along their hard axis (Fig. 2e). Figure 2f shows the variation of magnetic coercivity (H_c) in both field directions (i.e., $H \perp c$ - axis and $H \parallel c$ - axis) and anisotropic field with temperature. The anisotropic field (H_k), defined as the difference in saturation between in-plane and out-of-plane magnetic fields, reaches ~ 7.9 T at 2 K and ~ 3.8 T at 300 K. Such a high value of H_k suggests that Fe_3GaTe_2 has a very high magnetic anisotropy energy density with a very strong PMA. The coercive field (H_c) is also comparatively quite high along in-

plane direction as compared to out-of-plane direction. Both the H_c and H_K decrease with an increase in temperature approaching the Curie temperature of Fe_3GaTe_2 . Figure 2g illustrates AHE signals R_{xy} measured at varying out-of-plane angles (θ) between c-axis of sample and magnetic field. It can be noted here that the magnitude of AHE signal ($R_{xy}^{AHE} = \frac{R_{xy}(+H_S) - R_{xy}(-H_S)}{2}$) remains almost constant till $\pm 80^\circ$; beyond that AHE loop disappears between ± 600 mT field range. Again, this indicates a strong out-of-plane magnetic anisotropy present in Fe_3GaTe_2 . Figure 2h shows the variation of AHE signals R_{xy} with positive and negative dc bias currents. We observed that the magnitude of anomalous Hall signal, the coercivity and saturation fields remains unchanged with positive or negative current bias varied between ± 0.1 mA to ± 1 mA, indicating the robustness of perpendicular anisotropic magnetic moment against dc current within these bias ranges.

2nd Harmonic nonlinear Hall effect and spin-orbit torque induced magnetization dynamics in $\text{TaIrTe}_4/\text{Fe}_3\text{GaTe}_2$ heterostructures

The harmonic Hall measurements are performed on $\text{TaIrTe}_4/\text{Fe}_3\text{GaTe}_2$ heterostructures to quantitatively evaluate the non-linear effects and magnetization dynamics driven by spin-orbit torque. When a sinusoidal current (I^ω) is applied to the vdW heterostructure composed of the spin-orbit material TaIrTe_4 and a ferromagnet Fe_3GaTe_2 , spin-orbit torques (τ_{SOT}) are generated on the magnetization (m) of the Fe_3GaTe_2 . This effect originates from the spin accumulation at the vdW interface due to efficient charge-spin conversion in TaIrTe_4 . Typically, two mutually orthogonal torques are generated: the damping-like torque ($\tau_{DL} \sim m \times (\sigma \times m)$) and the field-like torque ($\tau_{FL} \sim \sigma \times m$)^{9,30}.

In these measurements, the application of a sinusoidal current (I^ω) with a fixed frequency of 213.3 Hz induces SOT-driven magnetization oscillation, leading to the generation of different harmonics in both the longitudinal and transverse resistance signals. The 1st and 2nd harmonic signals are measured and analyzed across different angles (Φ_B)- representing the angle between the in-plane magnetic field ($H \perp c$) and applied sinusoidal current (I^ω) as well as under varying external magnetic fields (H_{ext}). This allows for the extraction of information about the current-induced effective SOT fields and torques.

Since, TaIrTe_4 exhibits both in-plane and out-of-plane spin polarizations (σ^{XY}, σ^Z), the applied I^ω along the a-axis of TaIrTe_4 generates both in-plane and out-of-plane components of the damping like ($\tau_{DL}^{XY}, \tau_{DL}^Z$) and field-like ($\tau_{FL}^{XY}, \tau_{FL}^Z$) torques. The 2nd harmonic transverse resistance generated from these current induced effective SOT fields ($H_{DL}^{XY}, H_{DL}^Z, H_{FL}^{XY}, H_{FL}^Z$) and torques ($\tau_{DL}^{XY}, \tau_{DL}^Z, \tau_{FL}^{XY}, \tau_{FL}^Z$) can be expressed as follows^{31,32},

$$R_{xy}^{2\omega} = R_{DL}^{XY} \cos \Phi_B + R_{DL}^Z \cos 2\Phi_B + R_{FL}^{XY} \cos \Phi_B \cos 2\Phi_B + R_{FL}^Z \quad (\text{Eq. 1})$$

Where:

$$R_{DL}^{XY} = H_{DL}^{XY} \frac{R_{AHE}}{2(H_{ext} + H_K)} + R_{ANE} + R_{ONE} H_{ext} \quad (\text{Eq. 2})$$

$$R_{DL}^Z = H_{DL}^Z \frac{R_{PHE}}{(H_{ext})} + R_{offset} \quad (\text{Eq. 3})$$

$$R_{FL}^{XY} = H_{FL}^{XY} \frac{R_{PHE}}{(H_{ext})} + R_{offset} \quad (\text{Eq. 4})$$

$$R_{FL}^Z = H_{FL}^Z \frac{R_{AHE}}{2(H_{ext}+H_K)} + R_{offset} \quad (\text{Eq. 5})$$

Here, R_{AHE} and R_{PHE} represent the anomalous Hall and planar Hall resistance which can be estimated from 1st harmonic transverse resistance signal. The anomalous Nerst effect (R_{ANE}), ordinary Nerst effect (R_{ONE}) and R_{offset} denoted contribution from thermal and background effects.

Figure 3a displays the 1st and 2nd harmonic transverse Hall resistance R_{xy} signal as a function of magnetic field applied parallel to the sample surface ($H \perp c$) and perpendicular to the applied current. In the 1st harmonic R_{xy}^ω vs H , a hysteresis loop with a magnetic anisotropic field H_K of ~ 1.5 T is observed. The 2nd harmonics transverse Hall resistance signal $R_{xy}^{2\omega}$ varies with the external magnetic field applied parallel to sample surface and either perpendicular ($H_y, \Phi_B = 90^\circ$) or parallel ($H_x, \Phi_B = 0^\circ$) to the direction of current or a-axis of TaIrTe₄. These results are shown in Figures 3b and 3c. The resistance is a hyperbolic function of the field for $|H| > H_K$, however it becomes discontinuous for $|H| < H_K$.

Figure 3d and 3e show 2nd harmonics transverse resistance ($R_{xy}^{2\omega}$) versus H_y and H_x under different applied sinusoidal current densities ($J_{a.c.}$). The hyperbolic curvature sharpens with the increased current density. For $R_{xy}^{2\omega}$ vs H_y data at $\Phi_B = 90^\circ$, equation (1) indicated that only z-components of the SOT torques and fields contributing to the 2nd harmonics signal. Therefore, $R_{xy}^{2\omega}$ for $|H_x| > H_K$ is fitted with equation (6):

$$R_{xy}^{2\omega} = H_{DL}^Z \frac{R_{PHE}}{H_y} + H_{FL}^Z \frac{R_{AHE}}{2(H_y+H_K)} + R_{offset} \quad (\text{Eq. 6})$$

This allows calculation of H_{DL}^Z and H_{FL}^Z . Similarly, for $R_{xy}^{2\omega}$ vs H_x data ($\Phi_B = 0^\circ$), the previous extracted H_{DL}^Z and H_{FL}^Z values are used to determine H_{DL}^{XY} and H_{FL}^{XY} using equations (1-5). The extracted values of $H_{DL}^{XY}, H_{DL}^Z, H_{FL}^{XY},$ and H_{FL}^Z with different current densities $J_{a.c.}$ are shown in Fig. 3f and 3g. The slopes of $H_{DL/FL}$ vs $J_{a.c.}$ are found to be $H_{DL}^Z/J \sim 4.83$ mT per MAcm⁻², $H_{DL}^{XY}/J \sim 0.89$ mT per MAcm⁻², $H_{FL}^Z/J \sim 0.35$ mT per MAcm⁻² and $H_{FL}^{XY}/J \sim 1.96$ mT per MAcm⁻² (inset of Fig. 3f,g). Using equation (7), the SOT efficiency $\epsilon_{DL}^{Z/XY}$ are calculated³³:

$$\epsilon_{DL}^{Z/XY} = \frac{2eM_s \alpha t_{FM} H_{DL}^{XY/Z}}{\hbar J_{a.c.}} \quad (\text{Eq. 7})$$

Where e and \hbar are electronic charge and reduced Plank constant, respectively, t_{FM} is the thickness of the ferromagnetic layer and M_s is the value of saturation magnetization. Here, $\alpha = \lambda_{sd(FM)}/t_{FM}$ account for the finite spin diffusion length ($\lambda_{sd(FM)}$) of the ferromagnetic layer. The value of ϵ_{DL}^Z and ϵ_{DL}^{XY} are determined to be ~ 2.96 and ~ 0.54 , respectively, with Fe₃GaTe₂ having a thickness of ~ 50 nm (calculated

from the atomic force microscopic measurements (Supplementary Fig. S1) and M_s of 40.11 emu.g⁻¹, as measured by SQUID on Fe₃GaTe₂ crystals at room temperature⁸.

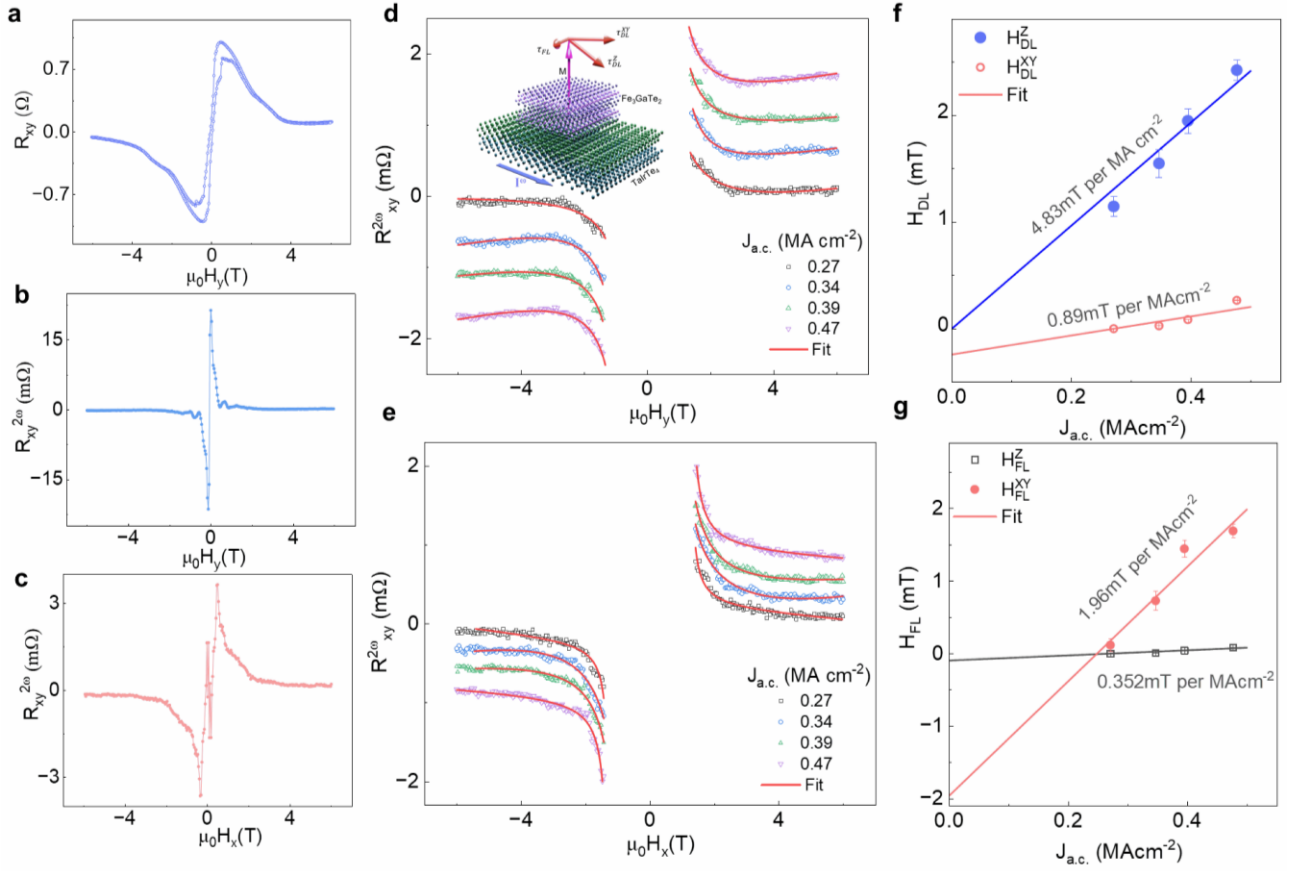


Figure 3. Field-dependent harmonic Hall measurements in TaIrTe₄/Fe₃GaTe₂ heterostructure. **a.** 1st harmonic transverse resistance ($R_{xy}^{1\omega}$) as a function of field swept parallel to sample surface ($H \perp c$) and perpendicular to current direction, measured at 300 K on Dev 1. **b,c,** 2nd harmonic transverse resistance $R_{xy}^{2\omega}$ varied as a function of the external magnetic field applied along parallel to samples surface, with H_y representing $H \perp c$ and perpendicular to the current ($H \perp J$), and H_x representing $H \perp c$ and parallel to the current ($H \parallel J$). **d,e,** Dependence of the 2nd harmonic transverse resistance $R_{xy}^{2\omega}$ on the in-plane magnetic field perpendicular (H_y) and parallel (H_x) to the current direction for different magnitudes of constant write current density. The inset depicts a schematic of the TaIrTe₄/Fe₃GaTe₂ heterostructure, illustrating the effects of damping-like torques (τ_{DL}^{XY} and τ_{DL}^Z) and field-like torques (τ_{FL}) on the magnetization of Fe₃GaTe₂ when the current is applied along the a-axis of TaIrTe₄ layer. **f,g,** Extracted field values corresponding to damping-like torques (H_{DL}) and field-like torques (H_{FL}) as a function of the write current density ($J_{a.c.}$), obtained from the fitting of the 2nd harmonic signal.

Field-free deterministic spin-orbit torque switching in TaIrTe₄/Fe₃GaTe₂ heterostructure

SOT magnetization switching experiments are crucial for investigating magnetization switching characteristics, such as determining the critical switching current density, assessing the need for an external field to aid in switching, and identifying whether the process is deterministic or non-deterministic. A series of pulse currents (I_{pulse}) applied along the a-axis in the TaIrTe₄/Fe₃GaTe₂ heterostructure can induce an unconventional spin current along the z-axis, with spin polarization σ_z oriented along the z-axis in TaIrTe₄²⁸. This spin current generates an unconventional SOT on Fe₃GaTe₂, consisting of both field-like (τ_{FL}) and damping-like (τ_{DL}) torques, facilitating the switching of the magnetization direction M . The field-like torque $\tau_{FL} \sim \sigma \times m$ induces the precession of M around the

exchange field generated by spin polarization, while the damping-like torque $\tau_{DL} \sim m \times (\sigma \times m)$ aligns M with the spin polarization σ , predominantly driving the magnetization switching (Fig. 4a)³⁴. Figure 4b shows the AHE at 300 K of Dev 2 used for switching experiments. Figure 4c presents SOT-induced magnetization switching, measured by applying a pulsed write current (I_p) along the a-axis with a pulse duration of 50 μ s. This is followed by a small DC read current ($I_r \sim 500 \mu$ A) to determine the magnetization state via the Hall resistance $R_{xy} = V_{xy}/I_r$. Due to a large unconventional SOT, fully deterministic field-free magnetization switching could be observed at room temperature with $I_p = \pm 3.5$ mA. Since the signal R_{xy} is proportional to the out-of-plane magnetization M_z , the SOT R_{xy} signal indicates a current-induced magnetization change between $+M$ and $-M$. Notably, deterministic SOT switching of TaIrTe₄/Fe₃GaTe₂ heterostructure is observed at $H_x = 0$ T, which indicates the creation of σ^z spin polarization in TaIrTe₄ with an out-of-plane SOT component. The magnitude of the switching signal is comparable to the AHE signal magnitude with field sweep, showing a full magnetization switching.

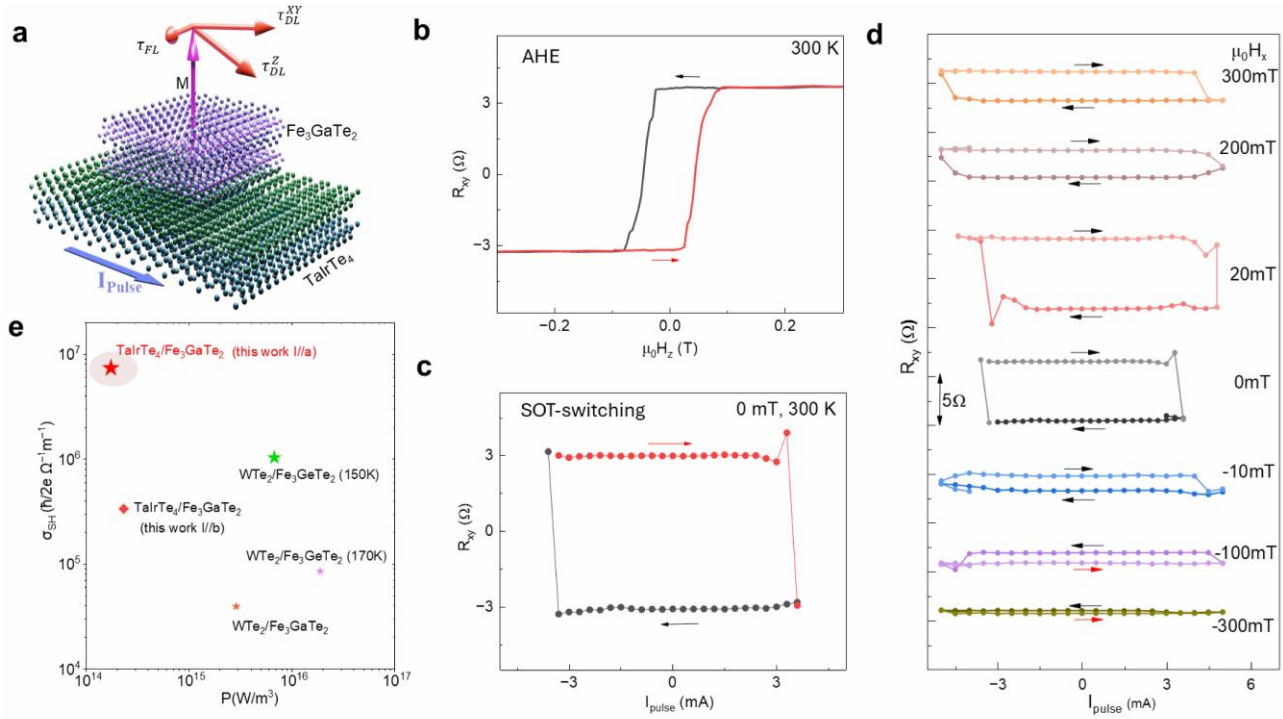


Figure 4. Energy-efficient, field-free deterministic magnetization switching by spin-orbit torque in the TaIrTe₄/Fe₃GaTe₂ heterostructure at room temperature. **a.** Diagrammatic representation of TaIrTe₄/Fe₃GaTe₂ heterostructure, illustrating how broken mirror symmetries and topological spin textures enable an out-of-plane component of spin accumulation at the TaIrTe₄/Fe₃GaTe₂ interface. This configuration leads to a significant out-of-plane antidamping torque (τ_{AD}^{OOP}), which is symmetric with respect to the current direction, facilitating field-free deterministic switching of the Fe₃GaTe₂ magnetization. **b.** AHE of the TaIrTe₄/Fe₃GaTe₂ heterostructure device 2 with magnetic field sweep at 300 K. **c.** Field-free full deterministic switching achieved at 3.5 mA pulse current and 500 μ A current is used as reading current to measure magnetization states keeping external field zero at 300 K temperature. The current is applied along the symmetry axis (a-axis) of TaIrTe₄. **d.** Current-driven magnetization switching of TaIrTe₄/Fe₃GaTe₂ under different bias fields parallel to the sample surface and current (H_x). **e.** Comparison of SOT spin Hall conductivity vs. power consumption with state-of-the-art results: our devices show more than one order of magnitude larger spin Hall conductivity with lower power consumption.

We further investigated the impact of deterministic SOT switching on the external in-plane magnetic field parallel to the current direction (Fig. 4d). The external in-plane magnetic field (H_x) can break the symmetry of deterministic SOT switching. As the strength of H_x increases, the switching mechanism transitions from being predominantly driven by the out-of-plane spin torque component (τ_{DL}^z) to being influenced by the in-plane components ($\tau_{DL}^{x,y}$). We observed that a small positive H_x has minimal effect on the SOT switching signal, however, increasing H_x beyond 100 mT results in a noticeable reduction of the signal magnitude. Despite this reduction, the switching efficiency was maintained at 50%, demonstrating some robustness against the external magnetic field. In contrast, when H_x is applied in the negative direction, the switching efficiency drops significantly to about 50% even at -10 mT, and it nearly diminishes to ~10% at -300 mT. Interestingly, the switching polarity remains unchanged up to 100 mT, indicating the effectiveness of the out-of-plane spin polarization of TaIrTe₄ in counteracting the external magnetic field^{12,28}. In conventional SOT, where magnetization switching is driven purely by in-plane spin current, the switching polarity typically reverses abruptly with H_x ^{29,35}. However, this was not observed in our experiments, highlighting the larger contribution of τ_{DL}^z from TaIrTe₄ in the magnetization dynamics of Fe₃GaTe₂. In device 3 (data provided in Supplementary Fig. S2), we observed that the switching polarity remained unchanged even up to 200mT when pulse current of ± 4 mA was applied along the a-axis of TaIrTe₄. However, it abruptly reversed when both the current and magnetic field of similar magnitude was applied along the b-axis of TaIrTe₄.

Furthermore, to examine the presence of τ_{DL}^z and calculate unconventional SOT driven switching efficiency, we have performed AHE loop shift measurement with bias current (see Supplementary Fig. S3)^{36,37}. The out-of-plane antidamping torque can shift the AHE hysteresis loop when a positive and negative dc bias current beyond a threshold value equivalent to switching current density is applied along the a-axis of TaIrTe₄. Such AHE loop shift (H_{shift}) is observed for compensating τ_{DL}^z driven intrinsic damping in Fe₃GaTe₂^{12,28,36}. The SOT efficiency (ϵ_{SOT}) due to unconventional τ_{DL}^z torque is defined by equation³⁷⁻³⁹

$$\epsilon_{SOT} = \frac{2eM_s\alpha t_{FM}}{\hbar} \frac{H_{shift}}{J_{switch}} \quad (\text{Eq. 8})$$

In our device, the ϵ_{SOT} is 3.95, with the H_{shift} and J_{switch} calculated to be 2 mT and $1.81 \times 10^{10} \text{ Am}^{-2}$, respectively. The switching efficiency parameter, defined as the ratio of switching current-driven and magnetic field-driven AHE, is observed to be 1 (Fig. 4c). Using the device parameter ($\epsilon_{SOT} = 3.95$ and charge conductivity $\sigma_c = 1.87 \times 10^6 \text{ S/m}$), we estimate the spin Hall conductivity to be $\sigma_{SH} = 7.39 \times 10^6 \hbar/2e (\Omega\text{m})^{-1}$. This value is attributed to the out-of-plane spin texture in TaIrTe₄ and spin transparency of the TaIrTe₄/ Fe₃GaTe₂ interface. By employing both SOT-induced magnetic switching and 2nd harmonic Hall measurements, we have established that the magnetization of Fe₃GaTe₂ in

heterostructure with TaIrTe₄ can be effectively manipulated with a switching current density of $J_{sw} \sim 1.81 \times 10^{10} \text{ A/m}^2$ and power density P of $0.175 \times 10^{15} \frac{\text{W}}{\text{m}^3}$ at room temperature. As benchmarked in Fig. 4e, the spin Hall conductivity σ_{SH} and power density P of TaIrTe₄/Fe₃GaTe₂ devices are an order of magnitude better than state-of-the-art field-free SOT devices^{10,12-14,28,35}, potentially leading to the advancement of energy-efficient spintronic devices.

Summary

In summary, we demonstrated the potential of TaIrTe₄/Fe₃GaTe₂ vdW heterostructures for generating a large nonlinear 2nd harmonic Hall effect and energy-efficient deterministic field-free magnetization switching at room temperature. By leveraging the unique properties of the topological Weyl semimetal TaIrTe₄ and the magnetic Fe₃GaTe₂ with strong PMA, our findings reveal a large non-linear Hall effect, substantial damping-like torque and a remarkably low switching current density, outperforming conventional systems. We observed a large 2nd harmonic Hall signal in TaIrTe₄/Fe₃GaTe₂ heterostructure at room temperature, which is found to be orders of magnitude higher than that of individual TaIrTe₄ and Fe₃GaTe₂ themselves. We measured a substantial damping-like torque of $4.83 \pm 0.59 \text{ mT per MAcm}^{-2}$ and observed deterministic field-free magnetization switching at a low current density of $1.81 \times 10^{10} \text{ A/m}^2$. The spin Hall conductivity σ_{SH} and power density P of TaIrTe₄/Fe₃GaTe₂ vdW heterostructure devices are an order of magnitude better than state-of-the-art field-free SOT devices, offering a promising route to energy-efficient and external field-free spintronic technologies.

Methods

Single crystal growth: TaIrTe₄ single crystals were synthesized by evaporating tellurium from a Ta-Ir-Te melt, with the crystal growth conducted at 850 °C and Te condensation at 720 °C⁴⁰. Fe₃GaTe₂ single crystals were grown via a self-flux method using Fe, Ga, and Te with 99.99% purity in the molar ratio of 1:1:2 in an evacuated and sealed quartz tube. The solid reactions took place for 24 hr at 1273 K, followed by cooling to 1153 K within 1 hr and slowly cooling down to 1053 K within 100 hr⁸.

Device fabrication: The van der Waals heterostructure samples were prepared by mechanically exfoliating nanolayers of TaIrTe₄ and Fe₃GaTe₂ crystals on top of each other on a SiO₂/Si wafer using the Scotch tape method inside a glove box. The top sample surface was immediately capped with a 2 nm Al₂O₃ layer to protect from degradation with time. The TaIrTe₄/Fe₃GaTe₂ heterostructures were patterned into Hall-bar geometry using electron-beam lithography (EBL) and Ar ion milling and Ti (15 nm)/Au (250 nm) contacts were prepared by EBL and electron beam evaporation.

Spin-orbit torque 2nd harmonic measurements: Spin-orbit torque was characterized using an in-plane 2nd harmonic Hall lock-in measurement technique. The $R_{xy}^{1\omega}$ and $R_{xy}^{2\omega}$ for an a.c. current I^ω of 213.3 Hz were simultaneously measured while rotating the sample in the plane (azimuthal angle ϕ_B) under an external field $\mu_0 H_{ext}$. The harmonic measurements were conducted using a Lock-in SR830 to detect the in-phase 1st and out-of-phase 2nd harmonic voltages. The 2nd harmonic measurements in the high magnetic field range were performed with a Quantum Design cryogen-free PPMS DynaCool system, interfaced with the SR830 to record the 1st and 2nd harmonic voltages. The 1st harmonic signal is detected by putting the voltmeter in phase with the oscillator, whereas the 2nd harmonic signal is out of phase with the source signal.

Spin-orbit torque switching measurements were conducted in a vacuum cryostat with a magnetic field strength of up to 0.7 T. Electronic measurements were carried out using a Keithley 6221 current source and a Keithley 2182A nanovoltmeter. To monitor the longitudinal and transverse Hall resistances, Keithley 2182A nanovoltmeters were employed. For SOT-induced magnetization switching, the Keithley 2182A nanovoltmeters were used to observe the Hall resistances responses, while a Keithley 6221 AC source applied a pulse current of 50 microsecond (μ s) through the device, followed by a DC read current of magnitude 500 μ A.

Acknowledgements

Authors acknowledge funding from European Union (EU) Graphene Flagship project 2DSPIN-TECH (No. 101135853), 2D TECH VINNOVA competence center (No. 2019-00068), Wallenberg Initiative Materials Science for Sustainability (WISE) funded by the Knut and Alice Wallenberg Foundation, EU Graphene Flagship (Core 3, No. 881603), Swedish Research Council (VR) grant (No. 2021-04821, No. 2018-07046), FLAG-ERA project 2DSOTECH (VR No. 2021-05925) and MagicTune, Graphene Center, Chalmers-Max IV collaboration grant, Areas of Advance (AoA) Nano, AoA Materials Science and AoA Energy programs at Chalmers University of Technology. The fabrication of devices was performed at Nanofabrication laboratory MyFab at Chalmers University of Technology.

Data availability

The data that support the findings of this study are available from the corresponding authors on a reasonable request.

Corresponding author

Correspondence to Saroj P. Dash (saroj.dash@chalmers.se)

Contributions

L.P., S.P.D. conceived the idea and designed the experiments. L.P. fabricated and characterized the devices with support from B.Z., R.N., L.S., H.B. and P.R. The TaIrTe₄ single crystals were grown by A.A. and M.A.H, while G.Z., H.W., and H.C. grew the Fe₂GaTe₃ single crystals. L.P. and S.P.D. analyzed and interpreted the experimental data and wrote the manuscript, with comments from all the authors. S.P.D. coordinated and supervised the project.

Competing interests

The authors declare no competing interests.

References

1. Manchon, A. *et al.* Current-induced spin-orbit torques in ferromagnetic and antiferromagnetic systems. *Rev. Mod. Phys.* **91**, 035004 (2019).
2. Shao, Q. *et al.* Roadmap of Spin–Orbit Torques. *IEEE Trans. Magn.* **57**, 1–39 (2021).
3. Han, W., Otani, Y. & Maekawa, S. Quantum materials for spin and charge conversion. *Npj Quantum Mater.* **3**, 27 (2018).
4. Liu, L. *et al.* Spin-Torque Switching with the Giant Spin Hall Effect of Tantalum. *Science* **336**, 555–558 (2012).
5. Gong, C. *et al.* Discovery of intrinsic ferromagnetism in two-dimensional van der Waals crystals. *Nature* **546**, 265–269 (2017).
6. Zhao, B. *et al.* Unconventional Charge–Spin Conversion in Weyl-Semimetal WTe₂. *Adv. Mater.* **32**, 2000818 (2020).
7. Zhao, B. *et al.* Observation of charge to spin conversion in Weyl semimetal WTe₂ at room temperature. *Phys. Rev. Res.* **2**, 013286 (2020).
8. Zhang, G. *et al.* Above-room-temperature strong intrinsic ferromagnetism in 2D van der Waals Fe₃GaTe₂ with large perpendicular magnetic anisotropy. *Nat. Commun.* **13**, 5067 (2022).

9. Zhao, B., Bainsla, L., Ngalyo, R., Svedlindh, P. & Dash, S. P. Coexistence of non-trivial van der Waals magnetic orders enable field-free spin-orbit torque switching at room temperature. Preprint at <http://arxiv.org/abs/2308.13408> (2023).
10. Kajale, S. N., Nguyen, T., Hung, N. T., Li, M. & Sarkar, D. Field-free deterministic switching of all–van der Waals spin-orbit torque system above room temperature. *Sci. Adv.* **10**, eadk8669 (2024).
11. Pan, Z.-C. *et al.* Room-temperature orbit-transfer torque enabling van der Waals magnetoresistive memories. *Sci. Bull.* **68**, 2743–2749 (2023).
12. Kao, I.-H. *et al.* Deterministic switching of a perpendicularly polarized magnet using unconventional spin–orbit torques in WTe₂. *Nat. Mater.* **21**, 1029–1034 (2022).
13. Shin, I. *et al.* Spin–Orbit Torque Switching in an All-Van der Waals Heterostructure. *Adv. Mater.* **34**, 2101730 (2022).
14. Highly Efficient Room-Temperature Spin–Orbit–Torque Switching in a Van der Waals Heterostructure of Topological Insulator and Ferromagnet. *Advanced Science* **11**, 2400893 (2024).
15. MacNeill, D. *et al.* Control of spin–orbit torques through crystal symmetry in WTe₂/ferromagnet bilayers. *Nat. Phys.* **13**, 300–305 (2017).
16. Shi, S. *et al.* All-electric magnetization switching and Dzyaloshinskii–Moriya interaction in WTe₂/ferromagnet heterostructures. *Nat. Nanotechnol.* **14**, 945–949 (2019).
17. MacNeill, D. *et al.* Thickness dependence of spin-orbit torques generated by WTe₂. *Phys. Rev. B* **96**, 054450 (2017).
18. Yang, H. *et al.* Two-dimensional materials prospects for non-volatile spintronic memories. *Nature* **606**, 663–673 (2022).
19. Bainsla, L. Large out-of-plane spin–orbit torque in topological Weyl semimetal TaIrTe₄. *Nat. Commun.* **15**, 4649 (2024).
20. Vila, M. *et al.* Low-symmetry topological materials for large charge-to-spin interconversion: The case of transition metal dichalcogenide monolayers. *Phys. Rev. Res.* **3**, 043230 (2021).
21. Liu, L. *et al.* Symmetry-dependent field-free switching of perpendicular magnetization. *Nat. Nanotechnol.* **16**, 277–282 (2021).
22. Kurebayashi, H., Garcia, J. H., Khan, S., Sinova, J. & Roche, S. Magnetism, symmetry and spin transport in van der Waals layered systems. *Nat. Rev. Phys.* **4**, 150–166 (2022).
23. Ma, J. *et al.* Nonlinear photoresponse of type-II Weyl semimetals. *Nat. Mater.* **18**, 476–481 (2019).
24. Jian, Y. *et al.* Transport signatures of temperature-induced chemical potential shift and Lifshitz transition in layered type-II Weyl semimetal TaIrTe₄. *2D Mater.* **8**, 015020 (2021).
25. Koepf, K. *et al.* TaIrTe₄: A ternary type-II Weyl semimetal. *Phys. Rev. B* **93**, 201101 (2016).
26. Kumar, D. *et al.* Room-temperature nonlinear Hall effect and wireless radiofrequency rectification in Weyl semimetal TaIrTe₄. *Nat. Nanotechnol.* **16**, 421–425 (2021).
27. He, P. *et al.* Bilinear magnetoelectric resistance as a probe of three-dimensional spin texture in topological surface states. *Nat. Phys.* **14**, 495–499 (2018).
28. Liu, Y. *et al.* Field-free switching of perpendicular magnetization at room temperature using out-of-plane spins from TaIrTe₄. *Nat. Electron.* **6**, 732–738 (2023).
29. Li, W. *et al.* Room-Temperature van der Waals Ferromagnet Switching by Spin-Orbit Torques. *Adv. Mater.* **35**, 2303688 (2023).

30. Miron, I. M. *et al.* Perpendicular switching of a single ferromagnetic layer induced by in-plane current injection. *Nature* **476**, 189–193 (2011).
31. Wu, H. *et al.* Room-Temperature Spin-Orbit Torque from Topological Surface States. *Phys. Rev. Lett.* **123**, 207205 (2019).
32. Bose, A. *et al.* Tilted spin current generated by the collinear antiferromagnet ruthenium dioxide. *Nat. Electron.* **5**, 267–274 (2022).
33. Shao, Q. *et al.* Role of dimensional crossover on spin-orbit torque efficiency in magnetic insulator thin films. *Nat. Commun.* **9**, 3612 (2018).
34. Zhu, L. Switching of Perpendicular Magnetization by Spin–Orbit Torque. *Adv. Mater.* **35**, 2300853 (2023).
35. Wang, H. *et al.* Room temperature energy-efficient spin-orbit torque switching in two-dimensional van der Waals Fe₃GeTe₂ induced by topological insulators. *Nat. Commun.* **14**, 5173 (2023).
36. Yu, G. *et al.* Switching of perpendicular magnetization by spin–orbit torques in the absence of external magnetic fields. *Nat. Nanotechnol.* **9**, 548–554 (2014).
37. Pai, C.-F., Mann, M., Tan, A. J. & Beach, G. S. D. Determination of spin torque efficiencies in heterostructures with perpendicular magnetic anisotropy. *Phys. Rev. B* **93**, 144409 (2016).
38. Nguyen, M.-H. *et al.* Enhancement of the anti-damping spin torque efficacy of platinum by interface modification. *Appl. Phys. Lett.* **106**, 222402 (2015).
39. Pai, C.-F., Ou, Y., Vilela-Leão, L. H., Ralph, D. C. & Buhrman, R. A. Dependence of the efficiency of spin Hall torque on the transparency of Pt/ferromagnetic layer interfaces. *Phys. Rev. B* **92**, 064426 (2015).
40. Chareev, D. A. *et al.* Growth of Transition-Metal Dichalcogenides by Solvent Evaporation Technique. *Cryst. Growth Des.* **20**, 6930–6938 (2020).